
Article:

Carcadea, E., Varlam, M., Ingham, D.B. et al. (2018) The effects of cathode flow channel size and operating conditions on PEM fuel performance: A CFD modelling study and experimental demonstration. International Journal of Energy Research, 42 (8). pp. 2789-2804. ISSN: 0363-907X

https://doi.org/10.1002/er.4068

The effects of cathode flow channel size and operating conditions on PEM fuel performance: a CFD modelling study and experimental demonstration

Elena Carcadea[a], Mihai Varlam[a], Derek B. Ingham[b], Mohammed S. Ismail[b], Laurentiu Patularu[a], Adriana Marinoiu[a], Dorin Schitea[a]

[a]National Research and Development Institute for Cryogenics and Isotopic Technologies - ICSI
Rm. Valcea, 240050, Romania
[b]Energy2050, Department of Mechanical Engineering, Faculty of Engineering, University of Sheffield, Sheffield S10 2TN, UK

Abstract

A comprehensive 3D, multiphase and non-isothermal model for a PEM fuel cell has been developed in this study. The model has been used to investigate the effects of the size of the parallel-type cathode flow channel on the fuel cell performance. The flow-field plate, with the numerically-predicted best performing cathode flow channel, has been built and experimentally tested using an in-house fuel cell test station. The effects of the operating conditions of relative humidity, pressure and temperature have also been studied. The results have shown that the fuel cell performs better as the size of the cathode flow channel decreases and this is due to the increased velocity which assists in removing liquid water that may hinder the transport of oxygen to the cathode catalyst layer. Further, the modelled fuel cell was found to perform better with increasing pressure, increasing temperature and decreasing relative humidity; the respective results have been presented and discussed. Finally, the agreement between the modelling and the experimentally data of the best performing cathode flow channel was found to be very good.

Keywords: PEM fuel cells; CFD modelling; channel size effects; operating conditions effects

1. Introduction

Proton Exchange Membrane (PEM) Fuel Cells are promising power sources for portable applications and this is due to their appealing features of low operating temperature, high efficiency and quick start up [1-4]. There have been many theoretical and experimental studies that have explored the effects of the design parameters and operating conditions on the performance of the PEM fuel cell; see for example [5-12]. The parameters are normally optimized to achieve the best possible fuel cell performance. For example, the relatively high and low humidity of the inlet gases could cause water flooding and membrane dehydration, respectively; therefore, the humidity of the inlet gases must be optimized to prevent the occurrence of the above two detrimental phenomena [13-16]. However, the optimization of the parameters influencing the fuel cell performance is not normally straightforward because of the interactions existing between them. For example, in order to achieve the optimum level of humidity, some other parameters, e.g. temperature and flow rate, should be controlled; therefore, such interactions must be taken into account in the optimization procedures [13].

Design-wise, there have been many numerical and experimental studies to investigate the effects of the flow channel geometry on the PEM fuel cell performance; see for example [16-20]. The effect of channel depth on the current distribution within the fuel cell was investigated numerically in [20]. Three channel depths were analysed, namely: 0.5, 1.0 and 1.5 mm. The results showed that the effect of the cathode channel depth was larger than that of the anode channel depth on the fuel cell performance. They also reported that the fuel cell with the shallowest channel, i.e. 0.5 mm, performs 10% better than that with deeper channels and this is due to the increased oxygen transfer rate to the active regions. However, compared to the deeper channels, the shallowest channel was found to significantly increase the pressure drop along the channel and cause a less uniform current distribution [20]. The non-uniform current density distribution may cause local hotspots, thus affecting the longevity and durability of the fuel cell. Therefore, the global (e.g. the overall performance degradation) and the local (e.g. hotspots) effects should be taken into account when investigating the sensitivity of the fuel cell to various parameters.

Numerical modelling is an efficient and cost-effective way to optimize the operating conditions and the design of the fuel cell as it significantly reduces the cost and time associated with the trial-and-error experimentation approach. There have been some studies in the literature in which the effects of the geometry of the flow channels have been numerically investigated and then corroborated with some experimental data; see for example [18] and [31]. Khazaee and Ghazikhani [18] numerically investigated the effects of the channel depth on the PEM fuel cell performance and they showed that it increases as the channel depth on either side of the fuel cell increases from 1 to 1.5 mm. Further, they showed that their numerical data for the cases in which the channels have been relatively deep are in good agreement with the corresponding experimental data taken from Miansari et al. [33]. Ferng et al. [31] experimentally and numerically investigated the effects of non-uniform channel depth on the performance of the fuel cell operating with either parallel or serpentine flow field plates. They found that the fuel cell performs better with the parallel flow field plates of non-uniform depth. However, they showed that the effects of non-uniform depth is almost negligible when using serpentine flow field plates. In this work, we first numerically investigate the effects of the width and depth of the cathode flow channel globally and locally. The best performing design for the cathode flow channel is subsequently used when investigating the sensitivity of the fuel cell to the operating conditions of relative humidity, temperature and pressure. Eventually, the best performing design of the cathode flow channel is manufactured and used in the operating fuel cell. Therefore, one of the important features of this investigation is that the design of the flow field plate has been led by a CFD modelling-based optimization study.

2. Model development

To be as comprehensive as possible, the model of the fuel cell has been set to be 3-diemnsional, multiphase and non-isothermal. Therefore, the transport phenomena in the modelled fuel cell are governed by the equations of conservation of mass, momentum, species, charge and energy. The current model is similar to the CFD model presented in a previous work [21] in which most of the governing equations were presented and described. As most of the governing equations were listed and described in [21], for brevity we only list these equations in Table 1 and we define their symbols in the nomenclature. Assuming unsaturated flow theory [22], the model in [21] was single phase and therefore the transport of liquid and dissolved water was not considered. In the following paragraphs, we therefore list and explain the governing equations associated with the transport of the liquid and the dissolved phases.

Three phases of water are present in the PEM fuel cell: gaseous, liquid and dissolved. The first two phases can be found in all the physical domains except the current collectors, and the third phase could be only present in the catalyst layers and the membrane. The water produced in the cathode catalyst layer is assumed to be in the dissolved phase [23].

[Insert Table 1]

The existence of all the water phases (i.e. gaseous, liquid and dissolved) and the mass transfer between them depend on the local thermodynamic and fluid dynamic conditions. There are three phase transfer mechanisms: condensation/evaporation between liquid water and water vapor, ionomer absorption between the dissolved water and water vapor, and ionomer desorption between the liquid water and dissolved water. The transport of the dissolved water in the ionomer (or membrane) phase is given as follows [23]:

$$\nabla \cdot \left(\vec{i}_m \frac{n_d}{F} M_{H_2O} \right) = \nabla \cdot \left(M_{H_2O} D_w \nabla \lambda \right) + S_\lambda + S_{gd} + S_{ld} \tag{1}$$

where λ is the dissolved water content, n_d is the osmotic drag coefficient, D_w is the diffusion coefficient of the dissolved water content, S_λ is the water generation rate due to the cathode side reaction in the catalyst layer, S_{gd} is the rate of mass change between the gas and dissolved phases and S_{ld} is the rate of mass change between the liquid and dissolved phases. The mathematical definitions of all the parameter shown in Equation (1) are presented in Table 2.

[Insert Table 2]

Note that in Table 2 ρ_i is the dry ionomer or membrane density (kg/m^3), EW is the equivalent weight of the membrane (kg/mol), γ_{gd} and γ_{ld} are the gas and liquid mass exchange rate constants, p_{wv} is the water vapor partial pressure (Pa), and $\lambda_{s=1}$ and $\lambda_{a=1}$ are the water content at saturation and water activity of unity, respectively.

Since water is generated in a dissolved form at the catalyst surface, it depends on the level of gas phase saturation if the water leaves the dissolved phase as a gas or as a liquid. If the gas phase is not saturated, then water will leave the dissolved phase as vapor at the catalyst surface. On the other hand, if the gas phase is saturated, then water will leave the dissolved phase as liquid at the catalyst surface which will be mainly removed by capillary diffusion.

The model also takes into account the transport of liquid water. The driving force of the liquid water transport is the liquid pressure gradient (∇p_l) [25]. Taking into account that the liquid pressure is the sum of the capillary pressure p_c and gas pressure p, the transport equation for the liquid water inside the porous electrodes and membrane can be given as follows [26]:

$$\nabla \cdot \left(\frac{\rho_l K K_r}{\mu_l} \nabla \left(p_c + p \right) \right) = S_{gl} \tag{2}$$

where ρ_l is the density of liquid water, μ_l is the dynamic viscosity of liquid water, K is the absolute permeability, K_r is the relative permeability and S_{gl} is the rate of mass change between gas and liquid phases. The mathematical expressions of the parameters shown in Equation (2) are listed in Table 3. On the other hand, the liquid water in the flow channels is governed by the following equation [26]:

$$\nabla \cdot \left(\rho_l \vec{v}_l s\right) = \nabla \cdot \left(D_{liq} \nabla s\right) \tag{3}$$

where D_{liq} is the liquid water diffusion coefficient in the channel, s is the water saturation and $\vec{v}_l$ is the liquid velocity which is assumed to be a fraction of the gas velocity $\vec{v}_g$ ($\vec{v}_l = \chi \cdot \vec{v}_g$, χ being the liquid to gas velocity ratio).

[Insert Table 3]

Numerical procedure and boundary conditions

All the above equations were solved using the Fuel Cell Module provided by the commercial numerical solver ANSYS Fluent 17.0 [26]. The coupled set of governing equations is iteratively solved until a converged solution is obtained, namely when the difference between two consecutive residuals is less than 10^{-6} and the difference between the current produced in the ACL and the CCL is less than 10^{-4}. These values have been found to be small enough as any smaller value does not show any graphical differences. Also, a few changes have been implemented in the solver options to attain a faster convergence, namely: the multigrid cycle was changed to the F-Cycle for all the equations and the stabilization method BCGSTAB (Bi-conjugate gradient stabilization) was chosen for the species concentrations, water saturation, electric and protonic potential [26]. The computations were performed using parallel processing of ANSYS Fluent with 32 processes shared on 2 workstations, each with two 8-core processors of 2.6 GHz and 64 GB of RAM. With these high performance computing (HPC) capabilities, the time required for simulating one point from the polarization curve was about 15 hours.

Since a single computational domain is used, the continuity in the fluxes of the various variables at the interfaces between the various components of the model is ensured. Dirichlet boundary conditions of constant mass flow rate, temperature, relative humidity and mass fractions were prescribed for the channel inlets; see Table 4. On the lateral walls of the modelled fuel cell, the solid phase potential was set to be 0 V at the anode side and between 0 and the open-circuit voltage (V_{oc}) at the cathode side. The V_{oc} in our simulations was that which we normally obtained from our fuel cell experiments, namely 0.95 V. It should be noted that the theoretical V_{oc} of PEM fuel cells operating with standard conditions of temperature 298 K and 1 atmospheric pressure is about 1.23 V [27]; however this is not achievable in practice due to gas cross-over and mixed potentials. Also, it worth noting that the mass fraction of hydrogen (i.e. 0.6) represents the amount of hydrogen that has been produced from the hydrolysis of the sodium borohydride.

[Insert Table 4]

The active area of the modelled fuel cell is 44 cm^2 (4.0 cm × 11.0 cm); this is based on the dimensions of a real fuel cell. The configurations of the flow field for the anode and the cathode sides are 3-pass serpentine and parallel, respectively; see Fig. 1. Each anode gas channel is 1.4 mm in width and 0.5 mm in depth. The dimensions of the cathode flow channel are the design parameters that are desired to be optimized to maximize the fuel cell performance; they have a significantly larger effect on the fuel cell performance than those of the anodic flow channel [15-20]. Therefore, the width and depth of the cathode flow channels have been realistically varied, resulting in 8 simulation cases; see Table 5. The widths of the rib at the anode and cathode flow channels are 1.3 and 1.0 mm, respectively. The number of the parallel flow channels at the cathode side was 44 when using the 1.5 mm channel width and 36 when using the 2.0 mm channel width. It should be noted that, upon calculating the respective Reynolds numbers, the flow for all the cases investigated was found to be laminar.

[Insert Table 5]

Gambit® software was used to build and mesh the computational domain. The mesh of the geometry, where the width and the depth of the cathode channels are 1.5 and 0.5 mm, respectively, is shown in Fig. 2. The mesh has been refined until mesh-independent solutions were obtained for all the cases; it was between 3.8 million cells for the 0.5 mm channel depth and 5.2 million cells for the 3 mm channel depth. The parameters used in the model are shown in Table 6. It should be noted that use of different flow field at the anode and cathode sides of the fuel cell has led to what is known as non-conformal interfaces at the mid-thickness of the membrane. The cell zones at these interfaces within the FLUENT platform are permitted to be connected to each other by passing fluxes from one mesh to another without any influence on the convergence of the solution [26].

Before the conclusion of this section, it is important to mention that the fuel cell investigated do not have a customary shape (square) and this is because the fuel cell being developed is based on a rectangular design, under an NDA contract with Baltic GmbH, in accordance with the portable military applications where they are intended to be used. The shape and the size of the fuel cells have been dictated by the amount of power required to power the military devices, taking into account that using short parallel flow channels at the cathode side allows an efficient removal of liquid water, thus facilitating the supply of oxygen to the reactive regions in the catalyst layer.

[Insert Table 6, Fig. 1 and Fig. 2]

3. Experimental investigation

The experimental work was performed using an in-house fuel cell test station; see Fig. 3. The 44 cm^2 PEM fuel cell has 12 mm thick aluminium compression plates and 2 mm gold-coated copper current collectors. The anode and cathode flow field channels were grooved into Schunk FU 4369 graphite plates. The GDLs used in the fuel cell are H24C3 (Freudenberg, Germany), and the MEA is from Baltic GmbH with 0.2 mg/cm^2 platinum loading at both the anode and the cathode electrodes.

The dry air and fuel are fed via a gas line (from pressurised cylinders), equipped with pressure gauges and flow controllers. Bubble humidifiers with an adjustable water level and temperature are used to humidify air and hydrogen streams. The pressure is set by using one-stage fix-value pressure regulator and a normal closed position valve mounted at the end of the gas line.

The polarisation curve of the fuel cell was constructed by setting several cell potentials between the open circuit voltage and 0.35 V and measuring the corresponding currents. This is performed by using a PLA800 60-300 electrical load bridge (AMREL American Reliance Inc., USA).

[Insert Fig. 3]

4. Results and discussions

From the polarization curves presented in Fig. 4, it can be seen that for high and medium operating voltages, the channel dimensions have a small influence on the performance, while at lower operating voltages the impact of the size of the channel on the performance begins to become significant. Namely, the fuel cell performs better as the channel depth and width decrease. This is in accordance with the results obtained by Wang et al. [10], Inoue et al. [20] and Wang et al. [30] which all show that the fuel cell performance improves as the dimension of the flow channel decreases. For a given flow rate, the velocity of the air increases as the dimensions of the flow channel decreases; higher velocities lead to better liquid water removal and (consequently) less flooded pathways between the channel and the catalyst layer, thus facilitating the supply of oxygen to the reactive sites in the cathode catalyst layer and improving the fuel cell performance. The improvement in the fuel cell performance with decreasing channel depth and width translates into more oxygen consumption and more water production as presented in Fig. 5 which shows the average oxygen and water concentration at the outlet of the cathode channel at 0.35 V. The 0.35 V cell potential was selected as it is the cell potential at which the differences between the simulation cases in terms of cell performance are more profound compared to other higher cell potentials. However, it should be noted that the fuel cell is normally operated at 0.6-0.7 V but at such potentials the variation between the simulation cases with the investigated parameters was shown to be almost negligible. It is also worth noting that, in order to be in line with the experimental data, there have been no simulations performed beyond 0.35 V.

[Insert Fig. 4 and Fig 5]

In addition to the global performance curves, it is important to analyse how the fuel cell performs locally. Namely, the profiles of the key variables within the components of the fuel cell could give insightful information on how uniform are the distributions of these variables. Less uniform distribution of some key variables, e.g. the current density and temperature, may lead to the presence of some undesirable phenomena such as hotspots, thus negatively affecting the lifetime and durability of the fuel cell. Fig. 6 shows the distribution of the current density at 0.35 V at the interface between the cathode catalyst layer and the MPL for all the investigated cases. It can be observed from the plots in Fig. 6 that the current density along the pathways from the inlet to the outlets decreases. This is directly linked to the distribution of the concentration of oxygen at the interface between the cathode catalyst layer and the adjacent MPL; see Fig. 7. As air travels from the inlets to the outlets, oxygen is consumed and becomes less available for reaction in the downstream regions of the active area, thus resulting in a smaller rate of current generation; this is evident from Faraday's law. One more general observation is that the current density is higher under the flow channels than under the ribs; this is due to the availability of more oxygen for reaction under the flow channel than under the rib at 0.35 V where the fuel cell is mainly limited by the rate of the transport of oxygen to the catalyst layer.

More importantly, the current density profiles in Fig. 6 shows that the current density becomes more uniform as the dimensions of the flow channels increase: the channels with 1.5 mm width and 0.5 mm depth present the least uniformity of the current density and the one with 2.0 mm width and 3.0 mm depth present the most uniformity of the current density. This is again attributed to how oxygen is distributed across the plane of interest; Fig. 7 shows that a less uniform distribution of oxygen is attained as the dimensions, in particular the depth, of the channel decrease. For a given flow rate, the smaller channels result in higher velocity and consequently higher rate of supply of oxygen to the active areas that are in particular beneath the flow channels. This will eventually lead to more disparity of the current between the areas under the flow channels and the areas under the ribs.

Fig. 8 shows the distribution of water at the interface between the cathode catalyst layer and the MPL. As expected, it follows the same uniformity trend as the oxygen distribution, namely: the channels with 1.5 mm width and 0.5 mm depth present the least uniformity and the one with 2.0 mm width and

3.0 mm depth present the most uniformity. More uniform distribution of water within the fuel cell assists in evenly humidifying the membrane and reducing the likelihood of presence of hotspots.

In conclusion, it can be seen that smaller dimensions of the channel gives the best fuel cell performance but least uniformity of the key variables. Therefore, care must be taken when optimizing the dimensions of the flow channels as significant non-uniformity of the local current density may cause some undesirable phenomena. This could be achieved through, for example, selecting the dimensions for the flow channel that are neither very small (to avoid hotspots and local dry-out of the membrane) nor very large (to avoid obtaining significantly reduced fuel cell performance due to the small contribution of the convection flow). It should be noted that, in addition to the insights provided by the CFD calculations, the fuel cell needs to be run under long-term operation in order to identify and confirm the best dimensions for the flow channels.

[Insert Fig. 6, Fig. 7 and Fig. 8]

In the next section, the effects of some of the key variables are investigated using the numerically best perfoming cathode flow channel, i.e. the one with 1.5 mm width and 0.5 mm depth.

Effects of relative humidity, temperature and pressure

In this section, the effects of the key variables of relative humidity, temperature and pressure on the fuel cell performance are analysed. The relative humidity is defined as the ratio between the partial pressure of the water vapor and the saturation pressure of the water vapor at a given temperature. Therefore, keeping the temperature at the inlet constant, the mixture composition at the anode/cathode inlet is varied in order to have a set of relative humidity (i.e. 35, 55 and 75%) through changing the temperatures of the bubble humidifier; the large is the temperature of the humidifier, the larger is the relative humidity. We have limited the relative humidity investigation to the cathode side as it, i.e. the cathode relative humidity, has a substantially greater effect on the performance of the fuel cell than that of the anode side [13]. It can be observed from Fig 9(a) that at high and medium voltages there is virtually no difference between the results. However, at low voltages, the fuel cell performs slightly better as the relative humidity decreases. This is in line with the findings of Lee and Hwang [29]. The reason behind this can be inferred from Fig. 9(b) and Fig. 9(c) which show the water mass fraction and saturation profiles at 0.35 V. As the relative humidity increases, the concentration of water vapor increases, especially in the downstream regions, thus resulting in an increased saturation (i.e. an increased presence of liquid water) and subsequently hindrance of transport of oxygen to the cathode catalyst layer. Therefore, for the given base operating conditions, it is preferred for the fuel cell investigated in this study to operate with relatively low humidity conditions at the cathode side.

[Insert Fig. 9]

Fig. 10 shows that, for the given base operating conditions, an increase in the cell operating pressure leads to a better performance [32]; the current at 0.35 V has increased by 17% as the operating pressure has increased from 1.0 to 1.5 atm. These results are in accordance with those presented in [28]. This is expected as higher operating pressure means the presence of more oxygen being available for reactions at the cathode catalyst layer, thus enhancing the rate of reaction as it is evident from Butler-Volmer equation. Therefore, if there are no technical constraints, relatively high cell operating pressure is recommended to be used to improve the fuel cell performance.

[Insert Fig. 10]

For the given base operating conditions, Fig. 11(a) shows that the fuel cell performs better as the temperature increases from 293 to 353 K; this is again in line with the results presented in [28]. This is mainly due to the positive effect of the temperature on the ionic conductivity of the membrane (Fig. 11(b)), and gas diffusivity (Fig. 11(d)). Such effects are evident from the Springer model [34] and the equation extracted from the Champan-Enskog theory [35] which both show that the membrane conductivity and gas diffusivity increase as the temperature increases, thus leading to less ohmic and concentration losses. Fig. 11(c) shows the distribution of the temperature at the interface between the cathode catalyst layer and the GDL. As expected and as it can observed from Fig. (b-d), the distributions of membrane conductivity and oxygen gas diffusivity are well correlated with the distribution of the temperature.

[Insert Fig. 11]

Experimental demonstration

The sensitivity of the fuel cell performance to the size of the cathode flow channel has been studied earlier. The relevant results showed that the fuel cell performs better as the cross-section of the channel decreases; the best performance was obtained with the channel of 1.5 mm width and 0.5 mm depth. A flow-field plate that houses the parallel flow channels of the latter dimensions have been subsequently manufactured and experimentally tested employing the fuel cell test station described in the Experimental Investigation Section and using the same base operating conditions. Fig. 12 shows the polarization curves obtained from the model and experiment for the cases 1 and 3 from the Table 5. The figure shows that the agreement between the modelling and experimental data is very good; the maximum difference between the two sets of data is about 6%. This imparts a high level of confidence on the CFD model built and its use as a design tool for any future improvements of the existing fuel cell. It should be noted that the only parameter that has been used to fit the numerical data to the experimental data was the cathodic charge transfer coefficient; the value that has given the best fit was found to be 0.8, which is in fact the average of the two values obtained experimentally for this parameter at high and low cell potentials [36, 37].

[Insert Fig. 12]

5. Conclusions

A CFD modelling study has been conducted to primarily investigate the sensitivity of the fuel cell performance to the width and depth of the parallel flow channels at the cathode side of a PEM fuel cell. The study has been extended to explore the effects of the operating conditions of the relative humidity, pressure and temperature on the modelled fuel cell performance. The CFD model built and used in the study was 3D, multiphase and non-isothermal. Further, the numerically best performance cathode flow channel was manufactured and in-situ tested. The following are the main findings of the study:

(i) The modelled fuel cell performs better as the size of the cathode flow channel decreases. For a given flow rate, the velocity increases as the cross-section of the flow channel decreases, thus improving the removal of liquid water and clearing the pathways for oxygen transport between the flow channel and the catalyst layer. However, small (shallow and narrow) flow channels may result in significant non-uniformity of the distribution of the current, oxygen and water within the MEA and potentially reduce the durability of the fuel cell. Therefore, care should be taken when optimizing the geometry of the flow channels.

(ii) For the given operating conditions, the modelled fuel cell was found to perform better with decreasing relative humidity. High relative humidity was found to result in higher liquid water saturation and subsequently increased hindrance of the transport of oxygen to the catalyst layer.

(iii) For the given operating conditions, the performance of modelled fuel cell was shown to increase with increasing operating pressure. This is attributed to the increase in the amount of oxygen available for reaction at the cathode catalyst layer. Likewise, the fuel cell performance was shown to improve with an increase in temperature and this is due to the enhancement of the ionic conductivity of the membrane phase and the diffusivity of the gases.

(iv) The agreement between the modelling and experimental data for the best performing cathode flow-field plate was found to be very good, imparting a confidence in the model built as design tool for future improvements.

Acknowledgments

This work has been funded by the Romanian Partnerships in priority domains – PNII Programme, from MEN-UEFISCDI, under the project no 284/2014.

Nomenclature

a	water activity
c	Concentration, mol/m^3
c_p	heat capacity, J/mol/K
D	diffusivity, m^2/s
F	Faraday's constant, C/mol
i	current, A
j	volumetric transfer current, A/m^3
j_0^{ref}	reference current density, A/m^2
k	thermal conductivity, W/m/K
K	absolute permeability, m^2
L	latent heat due to water condensation, J/kg
M	molecular weight, g/mol
R	universal gas constant, J/mol/K
S	source term
s	liquid water saturation
p	pressure, Pa
T	temperature, K
Y	mass fraction
v	velocity, m/s
V_{oc}	open circuit voltage, V

Greek symbols

α	charge transfer coefficient
ε	porosity
ζ	specific active surface area, 1/m
η	overpotential, V

μ	dynamic viscosity, Pa.s
φ	potential, V
ρ	density, kg/m^3
$\sigma_{sol/mem}$	electric/membrane conductivity, S/m
σ	surface tension (N/m)

Subscripts and superscripts

a/an	anode
c/cat	cathode
ref	reference
s/sol	solid
m/mem	membrane

Abbreviations

ACL	anode catalyst layer
CCL	cathode catalyst layer
CFD	computational fluid dynamics
CH	channel
CL	catalyst layer
GDL	gas diffusion layer
MEA	membrane electrode assembly
MPL	microporous layer
PEM	proton exchange membrane

References

1. Ay M, Midilli A, Dincer I, Exergetic performance analysis of a PEM fuel cell. Int J Energy Res 2005; 30:307-321.
2. Ismail MS, Borman DJ, Damjanovic T, Ingham D, Pourkashanian M. On the through-plane permeability of microporous layer-coated gas diffusion layers used in proton exchange membrane fuel cells. Int. J Hydrogen Energy 2011; 36:10392-10402.
3. Barbir F, Yazici S. Status and development of PEM fuel cell technology. Int J Energy Res 2008; 32:369-378.
4. Zang Z, Jia L. Parametric study of the porous cathode in the PEM fuel cell. Int J Energy Res 2009; 33:52-61.
5. Zamel N, Li X. A parametric study of multi-phase and multi-species transport in the cathode of PEM fuel cells. Int J Energy Res 2007; 32:698-721.
6. Shimpalee S, Van Zee J. Numerical studies on rib & channel dimension of flow-field on PEMFC performance. Int J Hydrogen Energy 2007; 32:842-856.
7. Kandlikar SG, See EJ, Banerjee R. Modeling two-phase pressure drop along PEM fuel cell reactant channels. J Electrochem Soc 2015; 162:F772-F782.
8. Ismail MS, Hughes KJ, Ingham DB, Pourkashanian M. Effect of PTFE loading of gas diffusion layers on the performance of proton exchange membrane fuel cells running at high-efficiency operating conditions, Int J Energy Res 2013;37:1592-1599.
9. Ratlamwala TAH, El-Sinawi AH, Gadalla MA, Performance analysis of a new designed PEM fuel cell. Int J Energy Res 2011; 36:1121-1132.
10. Wang XD, Yan WM, Duan YY, Weng FB, Jung GB, Lee CY. Numerical study on channel size effect for proton exchange membrane fuel cell with serpentine flow field. Energy Convers Manage 2010; 51: 959-968.
11. Jang W K, Choi J, Seo YH, Kim BH. Effect of cathode flow field configuration on air-breathing proton exchange membrane fuel cell. Int J Precis Eng Man 2015; 16:1129-1134.
12. Schmitz A, Tranitz M, Eccarius S, Weil A, Hebling C. Influence of cathode opening size and wetting properties of diffusion layers on the performance of air-breathing PEMFCs. J Power Sources 2006; 154:437-447.
13. Sanchez DG, Ruiu T, Friedrich KA, Sanchez-Monreal J, Verab M. Analysis of the influence of temperature and gas humidity on the performance stability of polymer electrolyte membrane fuel cells. J Electrochem Soc 2016; 163:F150-F159.

14. Chu D, Jiang R. Performance of polymer electrolyte membrane fuel cell (PEMFC) stacks: Part I. Evaluation and simulation of an air-breathing PEMFC stack. J of Power Sources 1999; 83:128-133.

15. Jeong SU, Cho EA, Kim HJ, Lim TH, Oh IH,Kim SH. Effects of cathode open area and relative humidity on the performance of air-breathing polymer electrolyte membrane fuel cells. J Power Sources 2006; 158:348-353.

16. Chiu HC, Jang JH, Yan WM, Li HY, Liao C. A three-dimensional modeling of transport phenomena of proton exchange membrane fuel cells with various flow fields. Appl Energy 2012; 96:359-370.

17. Kumar PM, Kolar AK. Effect of cathode design on the performance of an air-breathing PEM fuel cell. Int J Hydrogen Energy 2010; 35:671-681.

18. Khanzaee A, Ghazikhani M. Numerical simulation and experimental comparison of channel geometry on performance of a PEM fuel cell. Arab J Sci Eng 2012; 37:2297-2309.

19. Iranzo A, Rosa F, Pino J. A simulation tool for geometrical analysis and optimization of fuel cell bipolar plates: development, validation and results. Energies 2009; 2:582-594.

20. Inoue G, Matsukuma Y, Minemoto M. Effect of gas channel depth on current density distribution of polymer electrolyte fuel cell by numerical analysis including gas flow through gas diffusion layer. J Power Sources 2006; 157:36-152.

21. Carcadea E, Ingham DB, Stefanescu I, Ionete R, Ene H. The influence of permeability changes for a 7-serpentine channel pem fuel cell performance. Int J Hydrogen Energy 2011; 36:10376-10383.

22. Nam J, Kaviany M. Effective diffusivity and water-saturation distribution in single- and two-layer PEMFC diffusion medium. Int J Heat Mass Transfer 2003; 46:4595-4611.

23. Wang Y, Wang CY. Transient analysis of polymer electrolyte fuel cells. Electrochim. Acta 2005; 50:1307-1315.

24. Um S, Wang CY, Chen KS. Computational fluid dynamics modeling of proton exchange membrane fuel cells. J Electrochem Soc 2000; 147:4485-4493.

25. Scholz H. Modellierung und Untersuchung des Wärme- und Stofftransports und von Flutungsphänomenen in Niedertemperatur-PEM-Brennstoffzellen, PhD Thesis (2015).

26. ANSYS Multiphysics Help, www.ansys.com

27. Weber A Z, Newman J. Transport in polymer-electrolyte membranes: II. Mathematical Model. J Electrochem Soc 2004; 151: A311-A325.

28. Barbir F. PEM Fuel Cell: Theory and Practice, 2nd edition, Elsevier Academic Press; 2012

29. Lee P H, Hwang S S. Performance Characteristics of a PEM Fuel Cell with Parallel Flow Channels at Different Cathode Relative Humidity Levels. Sensors 2009; 9:9104-9121.

30. Wang C, Zhang Q, Shen S, Yan X, Zhu F, Cheng Z, Zhang J. The respective effect of under-rib convection and pressure drop of flow fields on the performance of PEM fuel cell. Sci Rep 2017; 7: 43447, doi: 10.1038/spre43447.

31. Ferng Y M, Su A, Lu S-M. Experiment and simulation investigations for effects of flow channel patterns on the PEMFC performance. Int J Energy Res 2008; 32:12-23.

32. Al-Baghdadi M A R S, Al-Janabi H A K S. Parametric and optimization study of a PEM fuel cell performance using three-dimensional computational fluid dynamics model. Renew Energy 2007; 32: 1077-1101.

33. Miansari Me, Sedighi K, Amidpour M, Alizadeh E, Miansari Mo. Experimental and thermodynamic approach on proton exchange membrane fuel cell performance. J. Power Source 2009; 190: 356-361.

34. Springer T E, Zawodzinski T A, Gottesfeld S. Polymer Electrolyte Fuel Cell Model. J Electrochem Soc 1991; 138: 2334-2342.

35. Chapman S, Cowling TG. The Mathematical Theory of Non-Uniform Gases, 3rd ed. Cambridge: Cambridge University Press; 1970.

36. Parthasarathy A, Srinivasan S, Appleby A J, Martin C R. Temperature Dependence of the Electrode Kinetics of Oxygen Reduction at the Platinum/Nafion® Interface—A Microelectrode Investigation. J Electrochem Soc 1992; 139: 2530-2537.

37. Sun W, Peppley B A, Karan K. An improved two-dimensional agglomerate cathode model to study the influence of catalyst layer structural parameters. Electrochim. Acta 2005; 50:3359-3374.

Table 1 The governing equations used in the model

Mass conservation equation:	
$\nabla\cdot\left(\varepsilon\rho\underline{v}\right)=S_m$	$S_m=\begin{cases}S_{H_2}+S_{H_2O} & \text{in ACL}\\ S_{O_2}+S_{H_2O} & \text{in CCL}\end{cases}$
Momentum equation:	
$\nabla\cdot\left(\varepsilon\rho\underline{v}\underline{v}\right)=-\varepsilon\nabla p+\nabla\cdot\left(\varepsilon\mu\nabla\underline{v}\right)+S_v$	$S_v=-\frac{\mu}{K}\varepsilon v$
Species transport equations:	
$\nabla\cdot\left(\varepsilon\underline{v}Y_i\right)=\nabla(D_i\nabla Y_i)+S_i$	$S_{H_2}=-\left(M_{H_2}/2F\right)\cdot j_\mathrm{a}$ $S_{O_2}=-\left(M_{O_2}/4F\right)\cdot j_\mathrm{c}$ $S_{H_2O}=\begin{cases}-M_{H_2O}\cdot\alpha & \text{in ACL}\\ M_{H_2O}\cdot\alpha+\left(M_{H_2O}/2F\right)\cdot j_c & \text{in CCL}\end{cases}$
where $\alpha=\frac{n_d\cdot j}{F}$	
Electron transport equation:	
$\nabla\cdot\left(\sigma_\mathrm{sol}\nabla\phi_\mathrm{sol}\right)=S_\mathrm{sol}$	$S_\mathrm{sol}=\begin{cases}-j_\mathrm{a} & \text{in ACL}\\ j_\mathrm{c} & \text{in CCL}\end{cases}$
Proton transport equation:	
$-\nabla\cdot\left(\sigma_\mathrm{mem}\nabla\phi_\mathrm{mem}\right)=S_\mathrm{mem}$	$S_\mathrm{mem}=\begin{cases}j_\mathrm{a} & \text{in ACL}\\ -j_\mathrm{c} & \text{in CCL}\end{cases}$
$\sigma_{mem}=\left(0.514\cdot\lambda-0.326\right)\cdot\exp\left(1268\cdot\left(1/303-1/T\right)\right)$	
Energy transport equation:	
$\nabla\cdot\left(\rho c_p\underline{v}T\right)=\nabla(k\nabla T)+S_T$	
$S_T=\begin{cases}i_s^2/\sigma_{sol}-S_{gl}\cdot L & \text{in GDL}\\ j_a\left(\eta_{an}-T\Delta S_{an}/2F\right)+i_s^2/\sigma_{sol}+i_m^2/\sigma_{mem}-\left(S_{ld}+S_{gl}\right)\cdot L & \text{in ACL}\\ j_c\left(-\eta_{cat}-T\Delta S_{cat}/2F\right)+i_s^2/\sigma_{sol}+i_m^2/\sigma_{mem}-\left(S_{ld}+S_{gl}\right)\cdot L & \text{in CCL}\\ i_m^2/\sigma_{mem} & \text{in membrane}\\ i_s^2/\sigma_{sol} & \text{in CC}\\ 0 & \text{in CH}\end{cases}$	

Closure relations:

$$j_a = \left(\zeta_a \cdot j_{0,a}^{ref}\right)\left(c_{H_2} \big/ c_{H_2}^{ref}\right)^{\gamma_a} \left[\exp\left(\alpha_a F \eta_{cat}/RT\right) - \exp\left(-\alpha_c F \eta_{cat}/RT\right)\right]$$

$$j_c = \left(\zeta_c \cdot j_{0,c}^{ref}\right)\left(c_{O_2} \big/ c_{O_2}^{ref}\right)^{\gamma_c} \left[-\exp\left(\alpha_a F \eta_{cat}/RT\right) + \exp\left(-\alpha_c F \eta_{cat}/RT\right)\right]$$

$$\eta_{an} = \phi_{sol} - \phi_{mem}$$

$$\eta_{cat} = \phi_{sol} - \phi_{mem} - V_{OC}$$

Table 2 The mathematical definitions of the parameters used in Equation (1).

Description	Expression
Osmotic drag coefficient, n_d (-)[24]	$n_d = 2.5\lambda / 22$
Diffusion coefficient of water content , D_w^i (m^2/s) [23]	$D_w^i = \frac{\rho_i}{EW} \cdot 4.1 \cdot 10^{-10} \left(\lambda / 25\right)^{0.15} \left[1 + \tanh\left(\lambda - 2.5 / 1.4\right)\right]$
Volumetric source term for dissolved water content, S_λ (kg/m^{3}s) [25]	$S_\lambda = M_{H_2O} \cdot j_{cat} / 2F$
Rate of mass change between gas and dissolved phases, S_{gd} (kg/m^{3}s) [25]	$S_{gd} = (1-s)\gamma_{gd} M_{H_2O} \frac{\rho_i}{EW}\left(\lambda_{eq} - \lambda\right)$
Rate of mass change between liquid and dissolved phases, S_{ld} (kg/m^{3}s) [25]	$S_{ld} = s\gamma_{ld} M_{H_2O} \frac{\rho_i}{EW}\left(\lambda_{eq} - \lambda\right)$
Equilibrium water content, λ_{eq} (mol H_2O/mol SO_3H) [25]	$\lambda_{eq} = 0.3 + 6a\left(1 - \tanh\left(a - 0.5\right)\right) + 0.69\left(\lambda_{a=1} - 3.52\right)a^{0.5} \cdot$ $\cdot \left(1 + \tanh\left(a - 0.89 / 0.23\right)\right) + s \cdot \left(\lambda_{s=1} - \lambda_{a=1}\right)$
Water activity, a (-) [24]	$a = p_{wv} / p_{sat}$
Saturation pressure, p_{sat} (Pa) [24]	$\log_{10} p^{sat} = -2.1794 + 0.02953 \cdot (T - 273.15) - 9.1837 \cdot$ $\cdot 10^{-5} \cdot (T - 273.15)^2 + 1.4454 \cdot 10^{-7} (T - 273.15)^3$

Table 3 The mathematical definitions of the parameters used in Equation (2).

Description	**Expression**
Relative permeability, K_r, [27]	$K_r = \begin{cases} s & in \quad GDL \\ \left(\dfrac{\dfrac{M_{H_2O}}{\rho_l}\lambda_{s=1} + \dfrac{EW}{\rho_i}}{\dfrac{M_{H_2O}}{\rho_l}\lambda + \dfrac{EW}{\rho_i}} \cdot \dfrac{\lambda}{\lambda_{s=1}} \right)^2 & in \quad membrane \end{cases}$
Rate of mass change between gas and liquid phases, S_{gl} [23]	$S_{gl} = \begin{cases} \gamma_{gl} \cdot \varepsilon \cdot s \cdot D_{gl} \dfrac{M_{H_2O}}{RT} p \ln\left(\dfrac{p - p_{sat}}{p - p_{wv}} \right) & p_{wv} \leq p_{sat} \\ \gamma_{gl} \cdot \varepsilon \cdot (1-s) \cdot D_{gl} \dfrac{M_{H_2O}}{RT} p \ln\left(\dfrac{p - p_{sat}}{p - p_{wv}} \right) & p_{wv} \rangle p_{sat} \end{cases}$
D_{gl} [25]	$D_{gl} = \begin{cases} 0.365 \cdot 10^{-4} \left(\dfrac{T}{343} \right)^{2.334} \cdot \left(\dfrac{10^5}{p} \right) & anode \\ 1.79 \cdot 10^{-4} \left(\dfrac{T}{343} \right)^{2.334} \cdot \left(\dfrac{10^5}{p} \right) & cathode \end{cases}$
Capillary pressure, p_c [25]	$p_c = \begin{cases} \sigma \cos\theta_c \sqrt{\dfrac{\varepsilon}{K}} \left(1.417(1-s) - 2.12(1-s)^2 + 1.263(1-s)^3 \right) & \theta_c < 90^\circ \\ \sigma \cos\theta_c \sqrt{\dfrac{\varepsilon}{K}} \left(1.417s - 2.12s^2 + 1.263s^3 \right) & \theta_c > 90^\circ \end{cases}$

Table 4 The boundary conditions used in the model.

Parameter	Value	Unit
Mass flow rate at anode inlet	3×10^{-6}	kg/s
Mass flow rate at cathode inlet	2×10^{-5}	kg/s
Mass fraction for H_2 at anode inlet (Y_{H_2})	0.6	-
Mass fraction for H_2O at anode inlet ($Y^a_{H_2O}$)	0.4	-
Mass fraction for O_2 at cathode inlet (Y_{O_2})	0.242	-
Mass fraction for H_2O at cathode inlet ($Y^c_{H_2O}$)	0.0699	-
Relative humidity at anode inlet	35%	-
Relative humidity at cathode inlet	55%	-
Temperature at anode and cathode inlets	333	K

Table 5 The depth and width of the cathode flow channel in the simulation cases.

Case number	**Depth (mm)**	**Width (mm)**
1	0.5	1.5
2	1.0	
3	1.5	
4	3.0	
5	0.5	2.0
6	1.0	
7	1.5	
8	3.0	

Table 6 The parameters used in the base case of the model.

Parameter	Value	Unit
Porosity of GDL/MPL/CL (ε)	0.7/ /0.5/0.4	-
Permeability of GDL/MPL/CL (*K*)	$2\times10^{-12}/1\times10^{-12}/2\times10^{-13}$	m^2
Reference exchange current density at anode (j_a^{ref})	10000	A/m^2
Reference exchange current density at cathode (j_c^{ref})	1	A/m^2
H_2 molar concentration ($c_{H_2}^{ref}$)	54.6×10^{-3}	$kmol/m^3$
O_2 molar concentration ($c_{O_2}^{ref}$)	3.39×10^{-3}	$kmol/m^3$
Anodic transfer coefficient (α_a)	0.5	-
Cathodic transfer coefficient (α_c)	0.8	-
Contact angle GDL/MPL/CL (θ_c)	110/110/95	^{o}
Anode/cathode specific surface area (ζ_{cat})	2×10^5	m^{-1}
Surface tension between gas and liquid phase (σ)	0.0625	N/m
Open circuit voltage (V_{oc})	0.95	V
Gauge pressure	1	atm
Membrane thickness	178	μm
GDL thickness	250	μm
MPL thickness	40	μm
Catalyst layer thickness	5.4	μm
Liquid water diffusion coefficient (D_{liq})	1×10^{-5}	m^2/s
Dry membrane density (ρ_i)	2000	kg/m^3
Equivalent weight of the membrane (*EW*)	1100	kg/kmol
Gas mass exchange rate constant (γ_{gd})	0.5	-
Liquid mass exchange rate constant (γ_{ld})	0.5	-
Water content at saturation ($\lambda_{s=1}$)	16.8	-
Water activity of unity($\lambda_{a=1}$)	9.2	-
Geometric factor of the droplet size (γ_{gd})	$1x10^8$	m^{-2}
Specific active surface area of catalyst (ζ)	200000	1/m
Liquid to gas velocity ratio (χ)	0.005	-

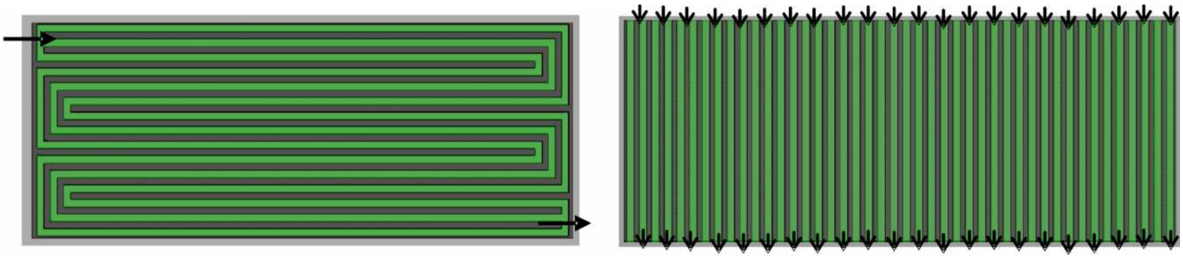

Fig. 1 The 3-pass anode serpentine flow channel (left) and parallel cathode flow channel (right).

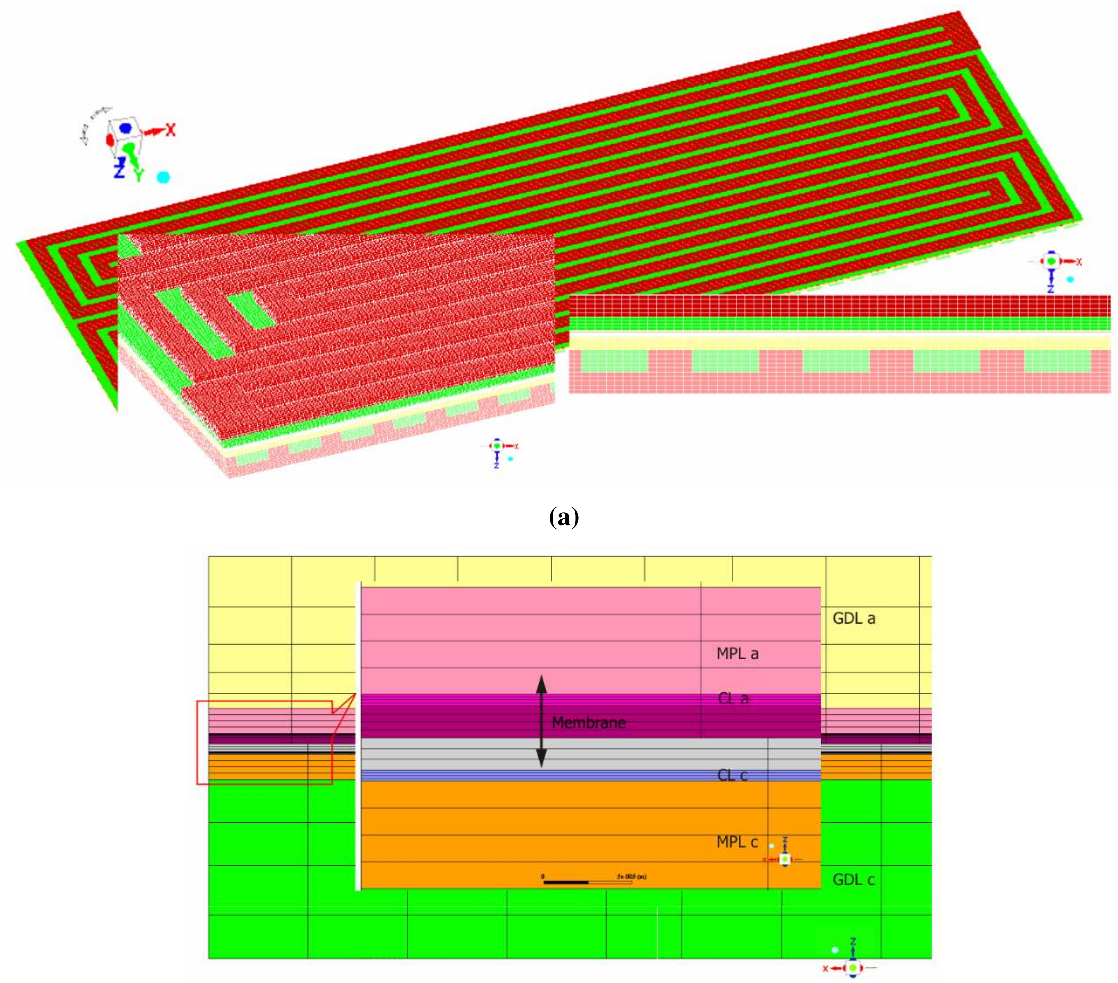

(a)

(b)

Fig. 2 (a) The meshed computational domain, and (b) zoomed-in view of the mesh of the MEA.

Table 6 The parameters used in the base case of the model.

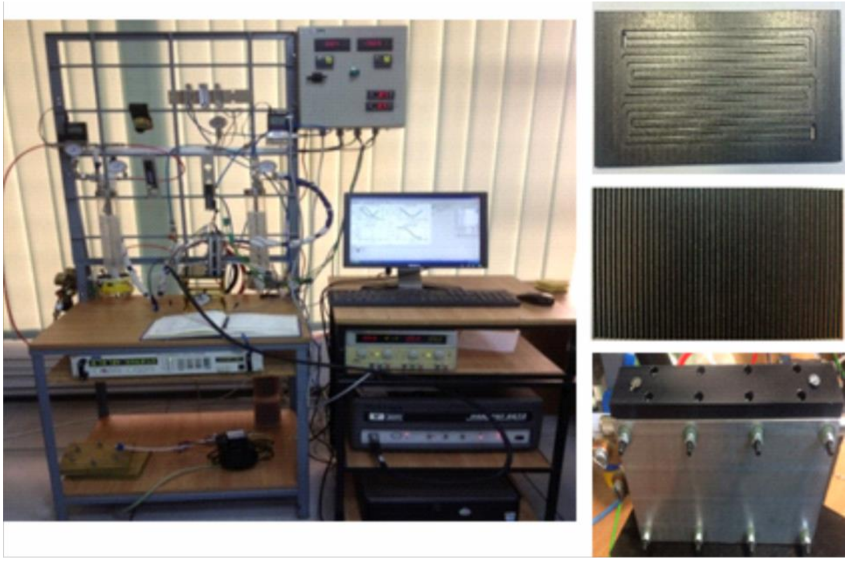

Fig. 3 Photograph of the fuel cell test station (left), anode flow-field plate, cathode flow-field plate and the housing of the fuel cell used (right).

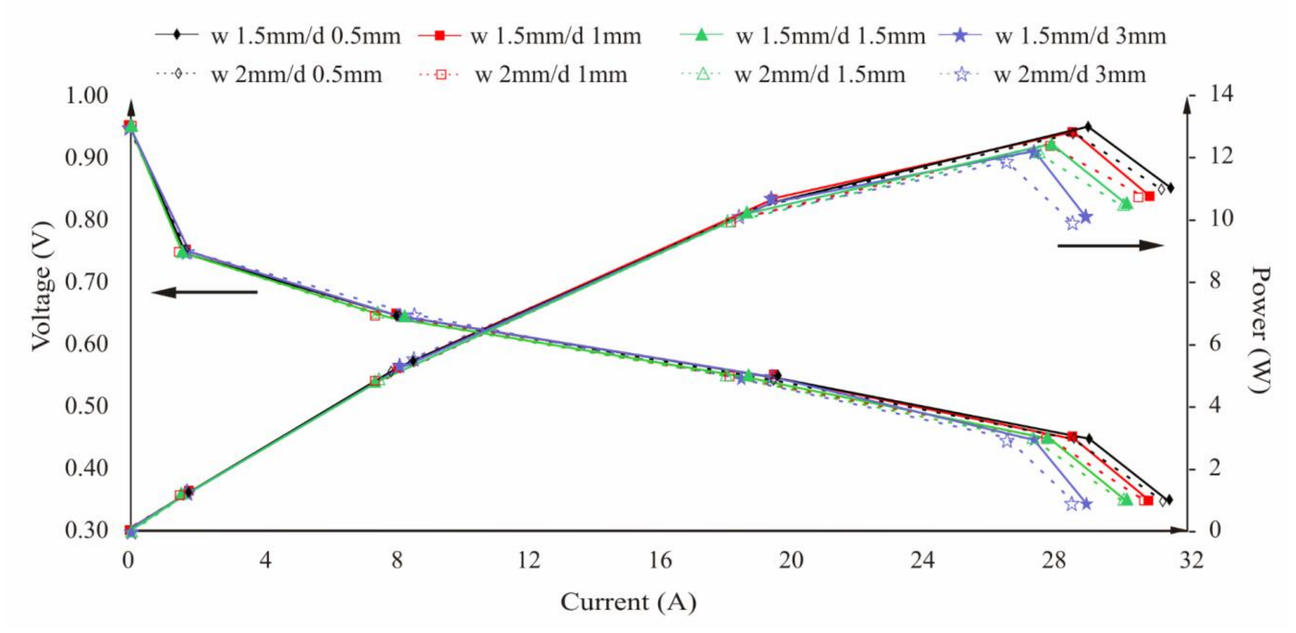

Fig. 4 The performance curves of the modelled fuel cell for various sizes of cathode flow channel.

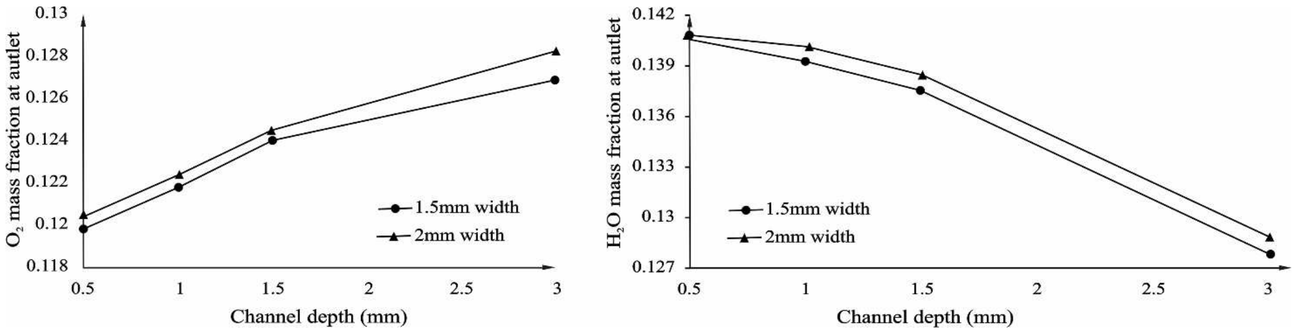

Fig. 5 (a) Oxygen mass fraction, and (b) water mass fraction at cathode channel outlet at 0.35V cell potential.

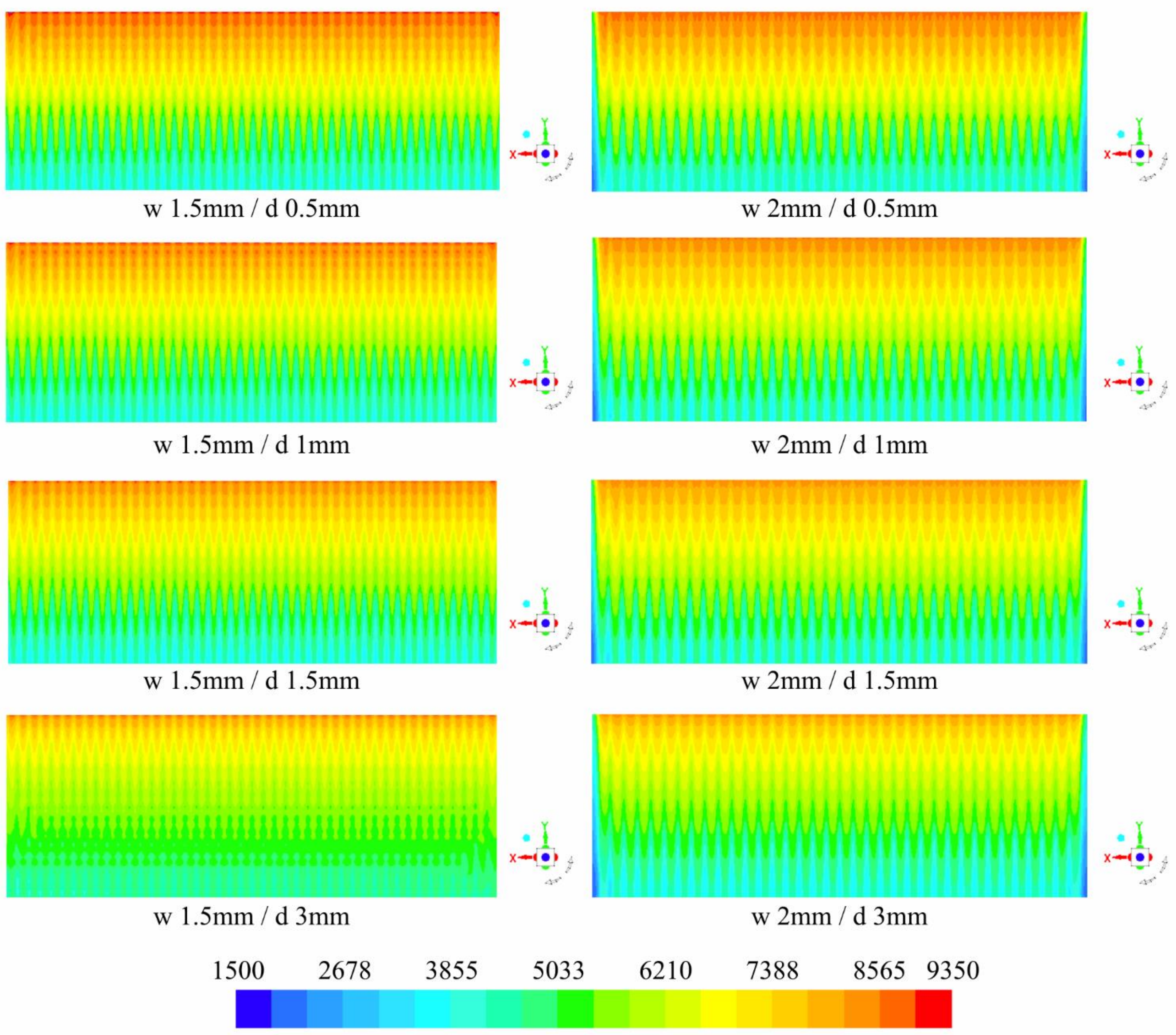
w 1.5mm / d 0.5mm

w 2mm / d 0.5mm

w 1.5mm / d 1mm

w 2mm / d 1mm

w 1.5mm / d 1.5mm

w 2mm / d 1.5mm

w 1.5mm / d 3mm

w 2mm / d 3mm

Fig. 6 The current density profile (A/m^2) at the interface between the CCL and MPL at 0.35V cell potential.

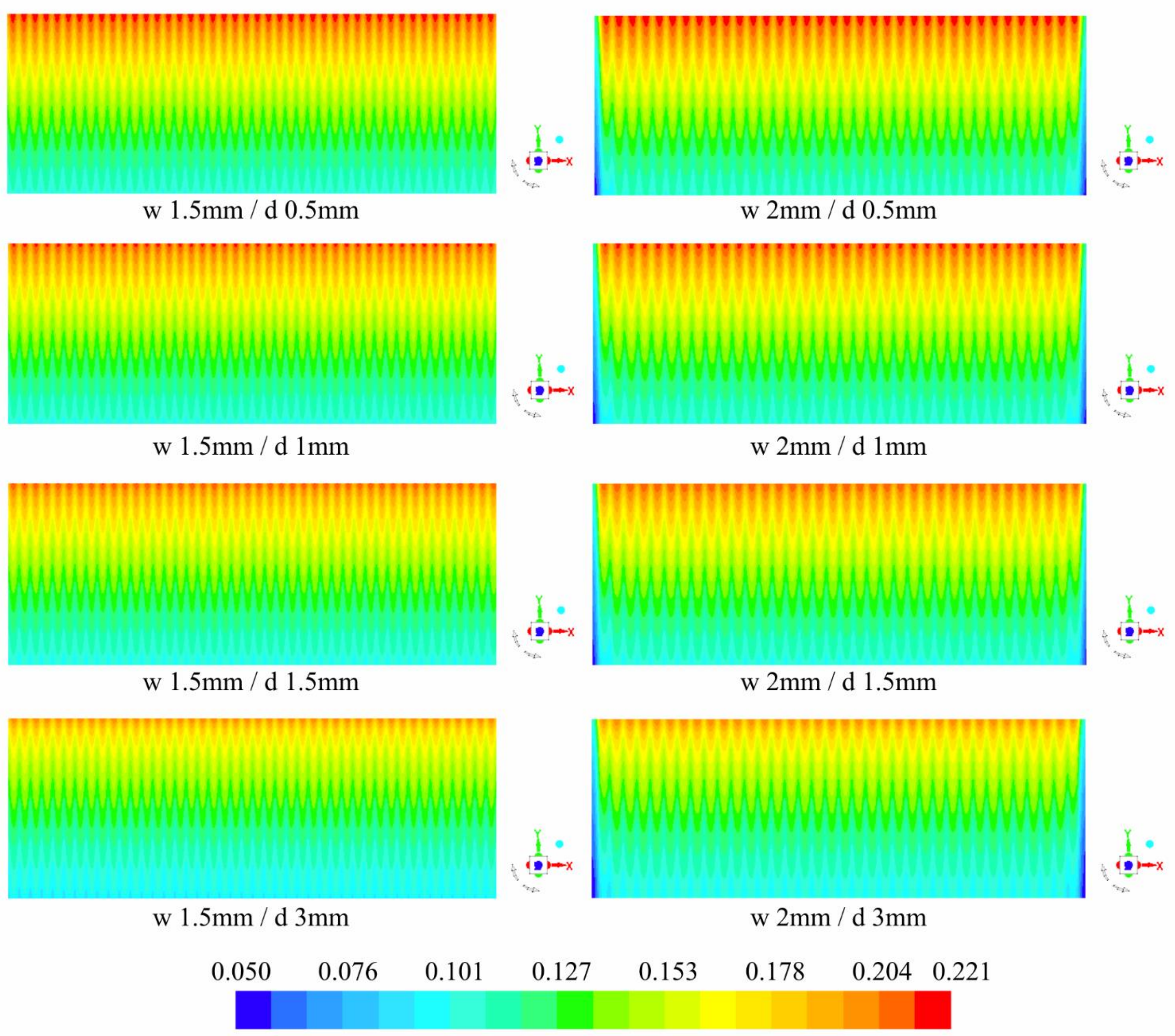
w 1.5mm / d 0.5mm

w 2mm / d 0.5mm

w 1.5mm / d 1mm

w 2mm / d 1mm

w 1.5mm / d 1.5mm

w 2mm / d 1.5mm

w 1.5mm / d 3mm

w 2mm / d 3mm

Fig. 7 The profile of oxygen mass fraction at the interface between the CCL and MPL at 0.35V cell potential.

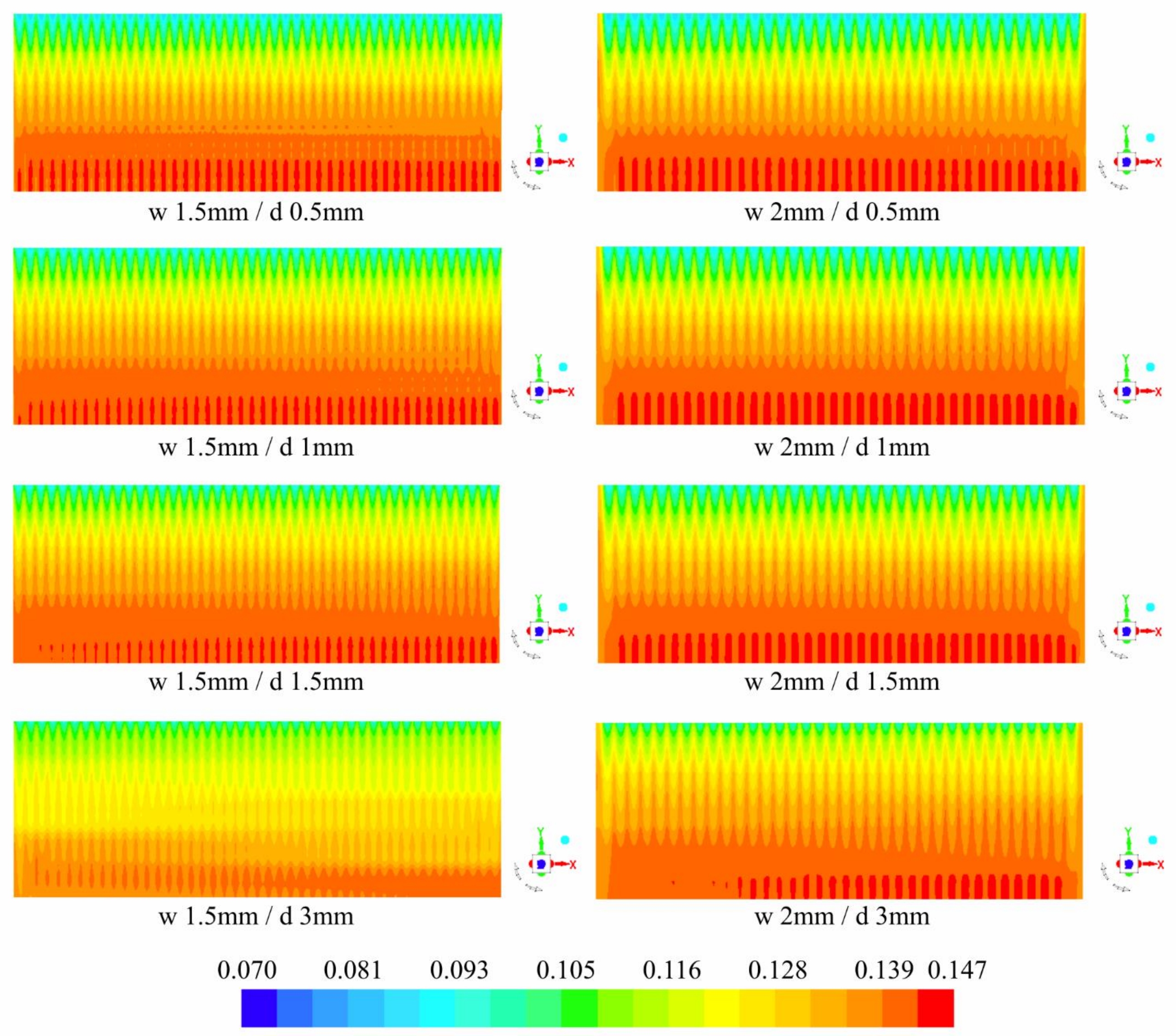
w 1.5mm / d 0.5mm

w 2mm / d 0.5mm

w 1.5mm / d 1mm

w 2mm / d 1mm

w 1.5mm / d 1.5mm

w 2mm / d 1.5mm

w 1.5mm / d 3mm

w 2mm / d 3mm

Fig. 8 The profile of water mass fraction at the interface between the CCL and MPL at 0.35V cell potential.

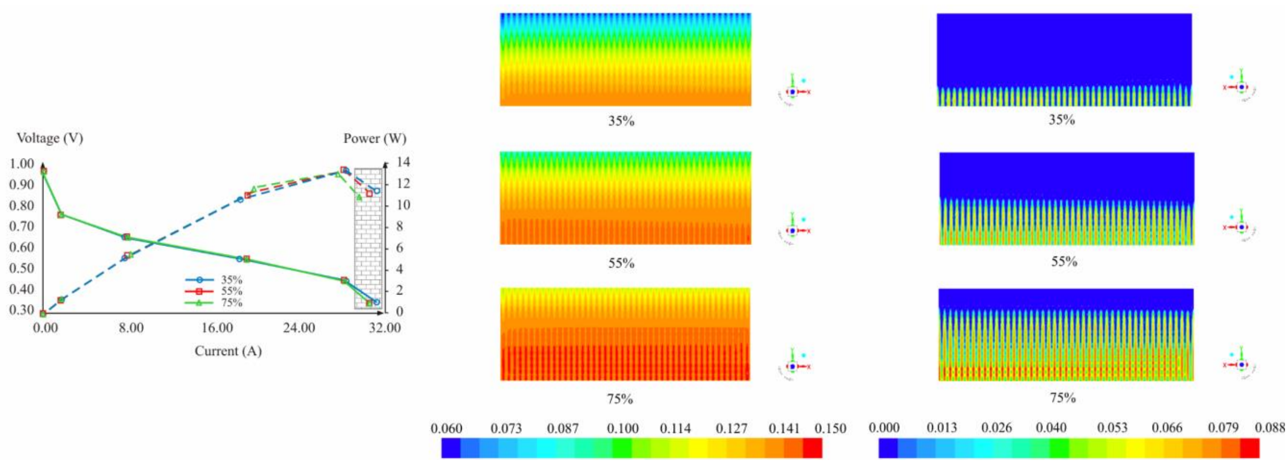

Fig. 9 (a) The fuel cell perfomance curves for the investigated inlet cathode relative humdity , (b) water mass fraction at the interface between the CCL and MPL at 0.35V, and (c) liquid water saturation at the interface between the CCL and MPL at 0.35V.

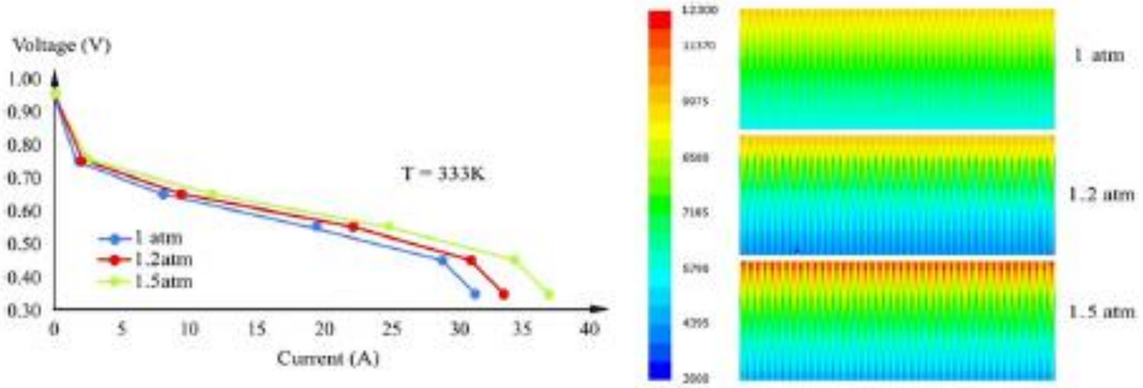

Fig. 10 The fuel cell polarisation curves as a function of operating pressure.

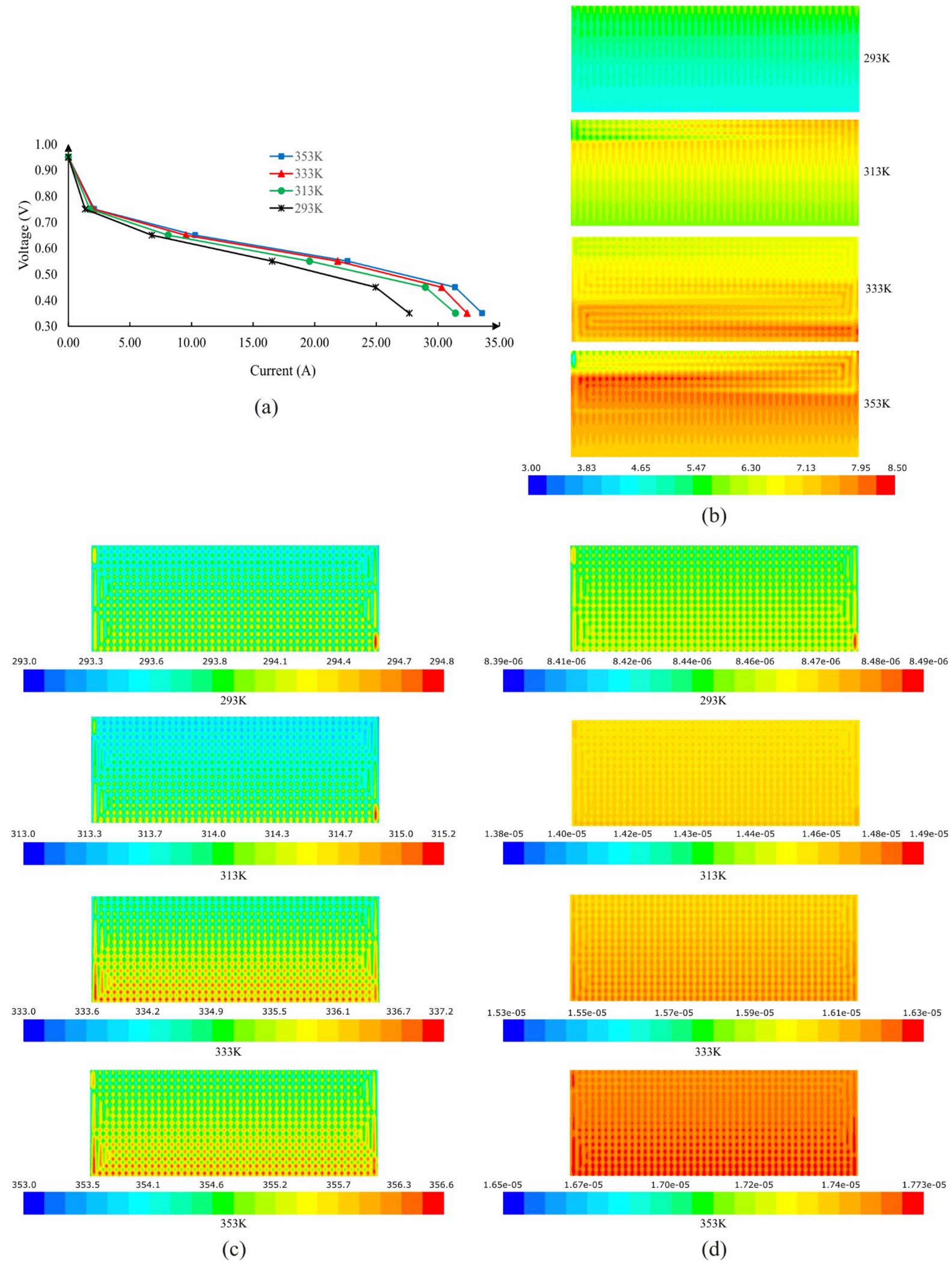

Fig. 11 (a) The fuel cell polarisation curves as a function of temperature, (b) the membrane conductivity (S/m) profile at the mid-thickness of the membrane, (c) the temperature profile at the mid-thickness of the membrane and (d) oxygen diffusivity (m^2/s) profile at the interface between the cathode GDL and the catalyst layer. Note that the cell potential at which the above profiles were computed was 0.35 V.

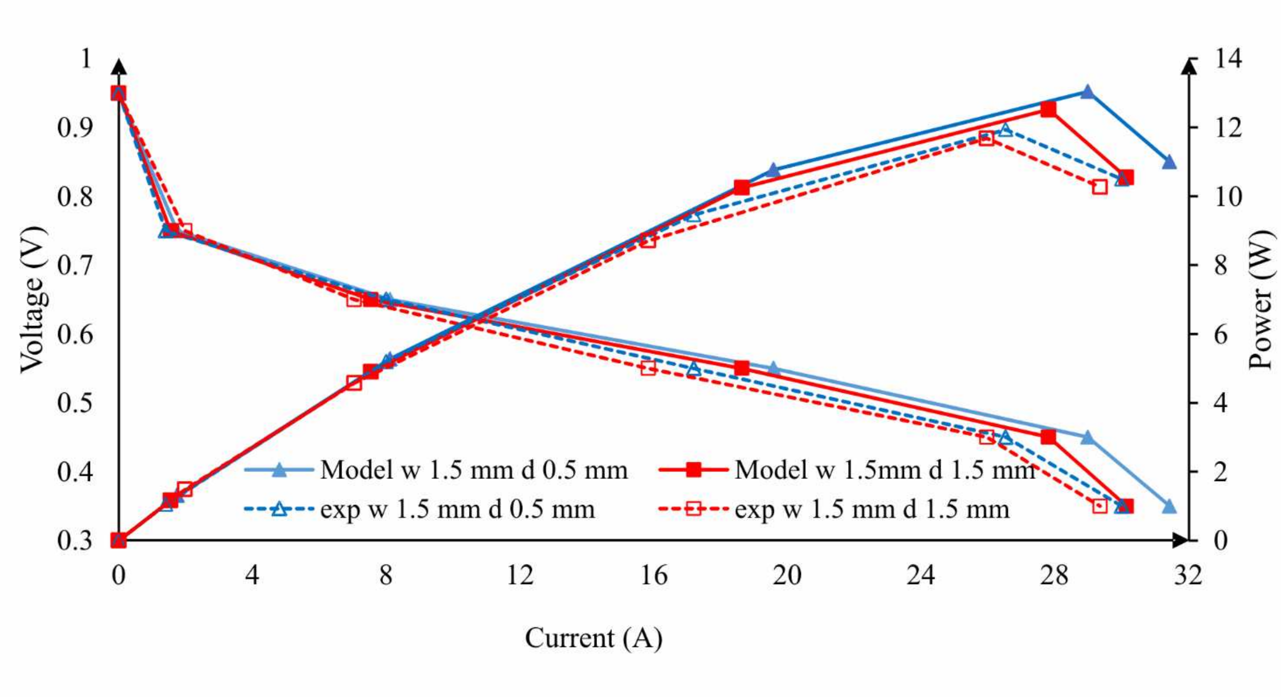

Fig. 12 The modelling and experimental performance curves.